Pergamon

Acta mater. 49 (2001) 4291–4311

Acta MATERIALIA

www.elsevier.com/locate/actamat

GRAIN LEVEL ANALYSIS OF CRACK INITIATION AND PROPAGATION IN BRITTLE MATERIALS

P. D. ZAVATTIERI‡[1] and H. D. ESPINOSA[2]†

[1]School of Aeronautics and Astronautics, Purdue University, West Lafayette, IN 47907-1282, USA and
[2]Department of Mechanical Engineering, Northwestern University, Evanston, IL 60208-3111, USA

(Received 26 March 2001; received in revised form 25 July 2001; accepted 25 July 2001)

Abstract—A study on the accuracy of cohesive models for capturing dynamic fragmentation of ceramic microstructures is presented. The investigation consists of a combined experimental/numerical approach in which microcracking and damage kinetics are examined by means of plate impact recovery experiments. The numerical analysis is based on a 2-D micromechanical stochastic finite element analysis. The model incorporates a cohesive law to capture microcrack initiation, propagation and coalescence, as well as crack interaction and branching, as a natural outcome of the calculated material response. The stochasticity of the microfracture process is modeled by introducing a Weibull distribution of interfacial strength at grain boundaries. This model accounts for randomness in grain orientation, and the existence of chemical impurities and glassy phase at grain boundaries. Representative volume elements (RVE) of ceramic microstructure with different grain size and shape distributions are considered to account for features observed in real microstructures. Normal plate impact velocity histories are used not only to identify model parameters, but also to determine under what conditions the model captures failure mechanisms experimentally observed. The analyses show that in order to capture damage kinetics a particular distribution of grain boundary strength and detailed modeling of grain morphology are required. Simulated microcrack patterns and velocity histories have been found to be in a good agreement with the experimental observations only when the right grain morphology and model parameters are chosen. It has been found that the addition of rate effects to the cohesive model results in microcrack diffusion not observed experimentally.

Keywords: Ceramics; Microstructure; Damage kinetics; Grain boundaries; Fracture & fracture toughness

1. INTRODUCTION

One of the problems in developing theories of ceramic microfracture is the lack of understanding of failure mechanisms and their evolution as a function of loading history. To advance the utilization of ceramics in applications where the possibility of dynamic loading exists, it is necessary to develop a theoretical framework accounting for deformation and failure under a variety of microstructurally-based mechanisms. Traditional models of inelastic deformation are based on volume averages of damage, stress and strain tensors, and bulk (volume averaged) elastic properties. A means for including material heterogeneity and stochastic variations in microstructure is required to properly capture failure. Dynamic failure as a result of nucleation, growth and coalescence of grain-boundary microcracks involves the cooperative interaction of propagating cracks. Insight into such processes is required from the perspective of material design and stochastic modeling of debonding of assemblies of grains.

Critical elements in the development of a physically-based model of the dynamic deformation and failure of ceramics requires experiments specifically designed to examine inelasticity. For instance, to study the initiation and evolution of microcracks in ceramics, an experiment that can cause controlled microcracking, under well defined stress conditions, was developed by Clifton and co-workers [1–6].

These investigators performed plate impact *soft recovery* experiments by subjecting the central region of a square ceramic specimen to known and controllable stress pulses. Microcracking resulted yet the specimens were recovered intact for microscopic analysis. Transmission electron microscopy (TEM) and scanning electron microscopy (SEM) observations of the recovered specimens revealed the formation of microcracks along grain boundaries. A

† To whom all correspondence should be addressed. Tel.: +1-847-467-5989; fax: +1-847-491-3915; http://www.mech.nwu.edu/espinosa.

E-mail address: espinosa@nwu.edu (H. D. Espinosa)

‡ Present address: General Motors Research & Development Center, 30500 Mound Road, Warren, MI 48090-9055, USA.

1359-6454/01/$20.00
PII: S1359-6454(01)00292-0

large portion of the microcracks was found to originate at triple points and both inelasticity in compression and tension was interferometrically measured. In the tension dominated region, several microcracks linked together to form a spall plane perpendicular to the impact direction. The presence of glass and/or impurities at some interfaces and triple points was identified as the principal source of damage initiation. By reducing the amount of glassy phase in the microstructure, they showed that tensile damage is less likely due to improved grain-boundary strength. These conclusions were tested on a high-purity, small-grain size alumina processed through hot pressing.

In spite of these contributions to the field of damage, lack of consensus on the mechanisms responsible for ceramic failure under multi-axial dynamic loading still remains [7]. Attempts have been made to model the inelastic constitutive behavior of ceramics in the presence of cracks, and to validate the models through simulation of plate and rod impact experiments. Available models for the failure of ceramics are continuum damage theories [7–13], which are based on homogenizing the cracked solid and finding its response by degrading the elasticity of the material. In addition, some of these models account for the initiation of cracks, coalescence, and friction between fragments in the comminuted zone. Continuum models have the limitation that they require assumptions on the size and distribution of microcracks to start with, and cannot describe the growth of dominant cracks leading to failure, a feature which is not suitable to homogenization.

Although there have been several models based on a discrete approach [14–18] which are able to nucleate cracks and follow their propagation and coalescence during the deformation process, the influence of microscopic heterogeneities on the overall material behavior, which depends on morphological characteristics such as size, shape, lattice orientation and spatial distribution of grains, is not accounted for.

Calculation of stress and strain distributions in real and idealized microstructures can increase the understanding of the different inelastic mechanisms controlling macroscopic response. Furthermore, these micromechanical simulations can be useful for quantification and determination of failure mechanisms, as well as the derivation of evolution equations to be used in continuum and discrete models [9, 11, 16]. In this way, bridging between length scales can be accomplished.

Several investigations on the microscopic response of the material have been carried out in the last decade [19–26]. The main characteristic of all these micromechanical models is their capability to include, in an explicit form, the heterogeneities of the material such as grain shape, size, and orientation, second phases, voids, flaws, etc. Despite all these developments in the area of micromechanics, bridging between micro and macro scales still remains one of the most challenging goals. Although in some cases comparison with micrographs of damaged specimens has been done, none of these studies has actually made a direct connection with experimental data leading to strong conclusions on the failure mechanisms and real macroscopic response of brittle materials.

In order to provide powerful tools to understand the mechanisms that lead to macroscopic failure and, at the same time, refine the theories of damage utilized in continuum or continuum/discrete models, a 2-D micromechanical model is presented to assess intergranular microcrack initiation and evolution. A representative volume element (RVE) of an actual microstructure, subjected to multi-axial dynamic loading, is considered for the different analyses. A large deformation elastic–anisotropic visco-plasticity model for the grains, incorporating grain anisotropy by randomly generating principal material directions, is included. Cohesive interface elements are embedded along grain boundaries to simulate intergranular fracture through microcrack initiation and evolution. Their interaction and coalescence are a natural outcome of the calculated material response.

This micromechanical model provides explicit account for arbitrary microstructural morphologies and microscopic fracture patterns making it easier to identify and design microstructural configurations that enhance fracture toughness, and therefore lead to improvements in the manufacturing of ceramic materials.

Through the consideration of actual microstructures, the effects of various fracture mechanisms can be delineated. The unique advantages of the micromechanical model proposed in this work include: (1) explicit account of real, arbitrary material microstructures, (2) explicit modeling of fracture in a non-constrained manner, therefore arbitrary crack paths or microcrack patterns are admitted, (3) direct analysis of the stochastic nature of fracture in heterogeneous microstructures, (4) consideration of the effect of residual stresses, (5) resolution of fracture over multiple length scales without limitations imposed by *ad hoc* fracture criterion; therefore, crack initiation, growth, coalescence and interaction are natural outcomes of material response, applied loading, and boundary constraints, (6) the representative computational cells where the calculations take place are chosen such that direct comparison with experimental data can be made.

Normal plate impact *soft-recovery* experiments have proven to be a powerful tool to induce microcracking in ceramics under well-known and controlled loading conditions without causing total failure of the specimen [1–5]. A detailed study of the damage initiation and kinetics in these experiments is carried out. The velocity profiles obtained from these experiments, which are very rich in information of damage kinetics, as well as SEM and TEM micrographs, make this experiment a good candidate for

the analysis of material failure in conjunction with the proposed micromechanical model under a fully dynamic framework. Measured and calculated velocity histories, as well as SEM micrographs and calculated crack patterns, are compared directly. The experiments not only provide constraints on the model parameters, but also they are useful in identifing and discriminating between different failure mechanisms. This approach avoids the drawback of most quasi-static experiments that capture only the end failure process due to unstable crack growth.

Analyzing the time history of failure is more important than taking a snapshot of the final outcome. While postmortem observations can reveal failure mechanisms such as intergranular and transgranular fracture and their relative proportions, they do not indicate the sequential order of the events. Additionally, postmortem observations do not necessarily provide information about fracture initiation and its evolution as a function of stress history.

Since experiments provide limited quantitative information on crack density, plasticity or twinning and their rate of change as a function of applied deformation rate, the implementation of an iterative computational/experimental procedure seems promising in this respect. The objective of this work is to provide tools and means to understand the macroscopic inelastic response of ceramics when subjected to dynamic multi-axial loading at the micron scale. This bridging between scales is achieved by a micromechanical stochastic finite element model. Experiments are not only used to examine and validate the micromechanical model but also to explain the different failure mechanisms.

2. MICROMECHANICAL MODEL

The finite element analysis of the initial boundary value problem is performed using a total Lagrangian continuum approach with a large deformation elastic and thermal anisotropic visco-plastic model [27, 28]. The elastic and thermal anisotropic model is used to describe grains' single crystal anisotropic behavior. The second Piola–Kirchhoff stress tensor relative to the undeformed configuration is described by $\mathbf{S}_{ij} = C_{ijkl}\mathbf{H}_{kl}$. Where $\mathbf{H}$ is a logarithmic strain measure or Henky strain, and C_{ijkl} is the elastic anisotropic material stiffness tensor in the global co-ordinates. Each grain is assumed to be elastic orthotropic and the orientation of the principal material directions differs from grain to grain. In order to keep the plane strain condition in the x–y plane, one of the principal material directions, which is chosen randomly, must coincide with the z-axis. The angle between the global axes x, y, and the two local axes lying in the plane x–y is also generated randomly. In general, this approach could be used for any orthotropic material where the normal to the three symmetry planes coincides with the local axes of co-ordinates, i.e. tetragonal systems: *Indium, tin, zircon*; transversely isotropic systems: *Cadmium, ice, zinc*; cubic: *Aluminum, copper, nickel, etc.*

A multi-body contact-interface algorithm is used to describe the kinematics at the grain boundaries and to simulate crack initiation and propagation. Figure 1 describes the contact model, integrated with interface elements to simulate microcracking at the grain boundaries and subsequent large sliding, opening and closing of the interface. The tensile and shear tractions in the zero thickness interface elements, embedded along grain boundaries, are calculated from the interface cohesive law. The interface cohesive law describes the evolution of these tractions in terms of both normal and tangential displacement jumps. Within the framework of cohesive interface elements the two most noteworthy cohesive failure models available in the literature are the potential-based law [17, 29, 30], and the linear law [14–16, 27].

The model assumes that the interface carries forces that oppose separation and shear between the surfaces until debonding. The magnitude of these forces is a function of the relative separation and shear displacements between the two surfaces. In formulating the cohesive law, a non-dimensional effective displacement jump is defined by

$$\lambda = \sqrt{\left(\frac{u_n}{\delta_n}\right)^2 + \xi^2\left(\frac{u_t}{\delta_t}\right)^2}$$

where u_n and u_t are the actual normal and tangential displacement jumps at the interface estimated by the finite element analysis, and δ_n and δ_t are critical values at which interface failure takes place. For a triangular $T-\lambda$ law, see Fig. 1, the normal and tangential components of the traction vector, in the range $0 \le \lambda \le \lambda_{cr}$, are given by

$$T_n = \frac{u_n}{\delta_n}\frac{T_{max}}{\lambda_{cr}};\ T_t = \alpha\frac{u_t}{\delta_t}\frac{T_{max}}{\lambda_{cr}}; \tag{1}$$

and for loading in the range $\lambda_{cr} < \lambda \le 1$,

$$T_n = T_{max}\frac{u_n}{\delta_n}\frac{1-\lambda}{\lambda(1-\lambda_{cr})};\ T_t = \alpha T_{max}\frac{u_t}{\delta_t}\frac{1-\lambda}{\lambda(1-\lambda_{cr})}. \tag{2}$$

T_{max} is the maximum normal traction that the interface can develop before failure and $\alpha = \xi^2(\delta_n/\delta_t)$ is the parameter coupling the normal and shear tractions, such that $\xi^2 = G_{IIc}/G_{Ic}$.

It is assumed here that the traction increases linearly to its maximum value $T = T_{max}$ when $\lambda = \lambda_{cr}$. Beyond λ_{cr}, the traction reduces to zero up to $\lambda = 1.0$ and any unloading takes place irreversibly [27, 28], which means that the interface between bodies is intact until the interface traction reaches the

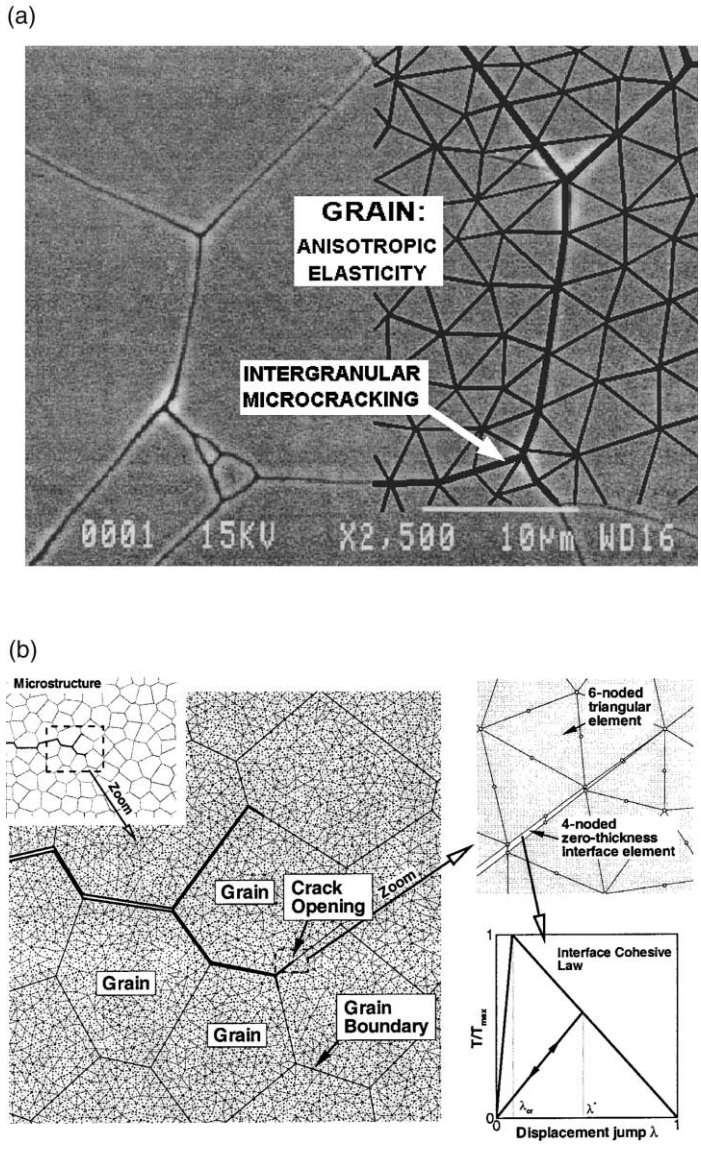

Fig. 1. Schematics of microcracking at grain boundaries using an irreversible interface cohesive law. Evolution of the traction with loading and unloading is also shown.

maximum value. Once the maximum traction is reached, the interface starts failing and the traction reduces to zero linearly up to the maximum displacement jump. From the values of fracture toughness K_{Ic}, or equivalently G_{Ic}, assuming plane strain, and the maximum interface stress, the critical interface displacement jump is computed by equating the area under the $T-\delta$ diagram to G_{Ic}. The compressive tractions at the grain boundaries are calculated either with the compressive part of the $T-\delta$ relationship or through the impenetrability condition employed in the contact model, depending on whether or not there are large displacements. More detail on this cohesive interface model can be found in [27, 28, 31].

3. SOFT-RECOVERY IMPACT EXPERIMENTS

The *soft-recovery* plate impact experiment has been described in detail by Raiser *et al*. [1–3], and Espinosa *et al*. [4,5]. The experiment uses an eight pointed start-shaped flyer plate that impacts a square ceramic specimen, subjecting the central octagonal region to a plane pulse. Figure 2(a) shows this soft-recovery normal impact configuration. A tensile pulse is originated from a gap between the specimen and the momentum trap upon reflection of the compressive pulse. The velocity–time profiles recorded at the rear surface of the momentum trap plate provide information on microcrack initiation and evolution.

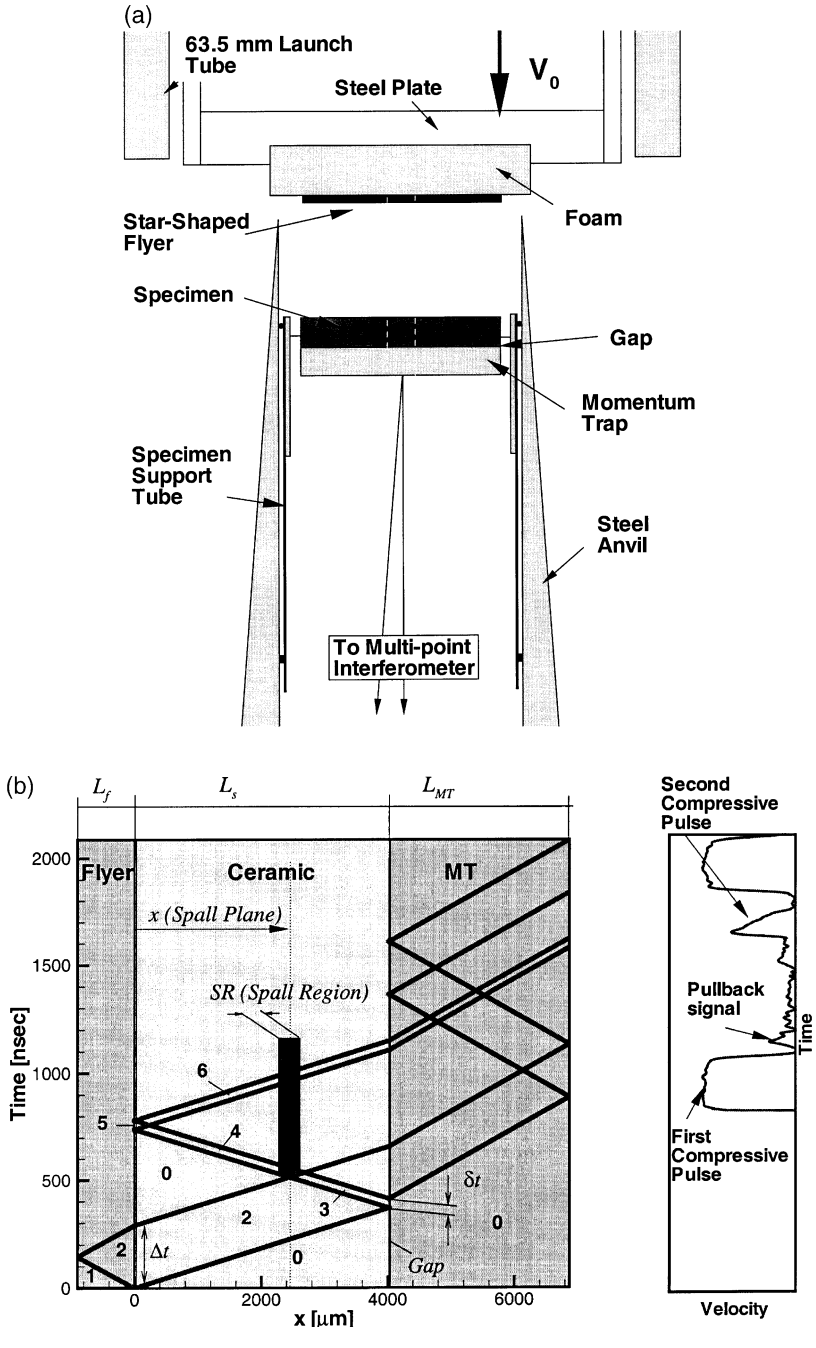

Fig. 2. (a) Soft-recovery normal impact configuration. (b) Lagrangian $t-X$ diagram for soft-recovery experiment.

Let x denote the distance from the front surface of the specimen measured in the direction of impact, and let L_s denote the thickness of the specimen, L_f the thickness of the flyer and L_{MT} the thickness of the momentum trap. The time–distance diagram resulting from a linear elastic analysis is shown in Fig. 2(b) as an aid in visualizing the conditions induced in the plates following impact.

The impact causes two compressive waves to emanate from the impacted surface, $x = 0$. One wave travels into the specimen causing a compressive stress, region 2 in Fig. 2(b). The other travels into flyer, reflects from the free surface and becomes a tensile pulse that unloads the compressive stress. This unloading wave proceeds into the specimen and removes the compressive stress there. The specimen, therefore, is subjected to a compressive pulse of a duration equal to the longitudinal wave's round-trip travel time through the start flyer. The rear surface of the specimen remains free of stress for as long as the gap between the specimen and momentum trap remains open. In order to maintain this traction-free

condition, the compressive pulse is reflected as a tensile pulse that crosses the compression region 2 and causes a zero stress state 3. This tensile pulse then propagates through the specimen causing tension over the region 4. The pulse then reflects from the impact surface of the specimen, becomes a compressive pulse, and proceeds through the specimen once more (region 6) before propagating into the momentum trap. The initial compressive pulse, minus the reflected part that causes the tensile pulse, travels through the momentum trap, reflects from the free surface and becomes a tensile pulse. When the tensile pulse reaches the interface between the specimen and the momentum trap, the latter separates from the specimen. The momentum trap flies off, leaving the specimen unstressed and with zero momentum. The particle velocity induced in the rear surface of the momentum trap is measured as a function of time by a normal displacement interferometer (NDI) and a normal velocity interferometer (NVI).

In the case of brittle materials readily damaged in tension, the tensile region 4 shown in Fig. 2(b) becomes the likely site of substantial damage called a *spall region*. Spallation can be defined as a complete or partial separation of material near the free surfaces resulting from the tension stress induced by the interaction of two waves, incident and reflected. When spallation initiates, the release waves emitted from the newly created free surfaces completely change the pattern of waves inside the specimen. The pull-back velocity measured right after the first compressive pulse, see velocity history in Fig. 2(b), is an indicator of damage kinetics. Since microcrack growth under the conditions of the experiment is found to be stable and because the duration of the tensile pulse can be controlled by varying the gap dimension, the progression of damage can be stopped before catastrophic failure of the specimen. In this manner, the specimen is recovered intact for subsequent inspection. Since the momentum trap remains elastic throughout the tests, the inelastic effects recorded can be attributed solely to inelastic processes within the specimen. A typical particle velocity recorded at the rear surface of the momentum trap showing the above features is shown in Fig. 2(b). The shape of the pull-back signal and second compressive pulse reflects both microcracking, under the tensile pulse itself, and attenuation while traveling through material already damaged. In the case in which there is no damage in the ceramic, there would not be pull-back signal and the second compressive pulse would be as high as the first and third compressive pulse. The above 1-D analysis is valid in the central region of the specimen, where the effects of diffracted waves from the corners and the edges of the flyer are minimized [4]. Espinosa *et al*. [32] demonstrated that the major perturbation to the 1-D response within the central region of the target plate results from spherical waves emanating from the corners of the star-shaped plate and that the observed damage within this region can be attributed primarily to the conditions arising from a state of uniaxial strain. The experimental findings suggested that the modeling of crack nucleation and growth requires consideration not only of the amplitude of the applied stress but also of its time dependence [4]. Several successful tests have been conducted using this experimental design by Espinosa *et al*. [4, 5] and Raiser *et al*. [1–3]. A summary of the shots used for comparisons with the proposed numerical model is presented later; see Fig. 3.

4. STOCHASTIC FEM SIMULATIONS

A representative volume element of an actual microstructure is considered for the analysis. Although the exact grain geometry can be taken from a digital micrograph, it is well established that the grain structure in polycrystalline materials can be simulated by a Voronoi tessellation [33]. We followed the last approach to generate enough statistical data. The large deformation elastic–anisotropic viscoplasticity model for the phases, incorporating grain anisotropy is included considering plane strain condition, as required for the interpretation of the plate impact experiments within a 2-D simulation. Cohesive interface elements are embedded along grain boundaries to simulate microcrack initiation and evolution. It should be noted that all experimental observations confirm that microcracks nucleate and propagate along grain boundaries. Within this model, microcrack interaction and coalescence is a natural outcome of the calculated material response. The tensile and shear traction in the interface elements are calculated from the interface cohesive laws described in [27].

In view of the plane strain conditions prevailing in the specimen and assuming periodicity, only a representative volume element of the ceramic is considered. Figure 4(a) shows a strip of the various plates used in the experimental configuration, only the flyer, momentum trap and specimen are considered in the analysis and due to the limited spread of tensile damage observed experimentally, only a small portion of the ceramic in the spall region is simulated. The top and bottom boundaries of the cell are modeled using viscous boundary conditions which represent the exact elastic wave solution along characteristic lines [32]. Here the assumption is that outside the spall region, the ceramic remains elastic with average elastic properties. This assumption is correct when the primary damage mode within the specimen is spallation, i.e., low impact velocities [4]. Higher impact velocities would require the study of the entire strip shown in Fig. 4(a) and would therefore imply a much heavier computational effort. Details on the boundary conditions and convergence can be found in [28, 33].

The elastic stiffness constants, C_{IJKL}, of a single crystal alumina [34] are: $C_{11} = C_{22} = 465$ GPa, $C_{12} = 124$ GPa, $C_{13} = C_{23} = 117$ GPa, $C_{33} = 563$ GPa, $C_{44} = (C_{11} - C_{12})/2$ and $C_{55} = C_{66} = 233$ GPa.

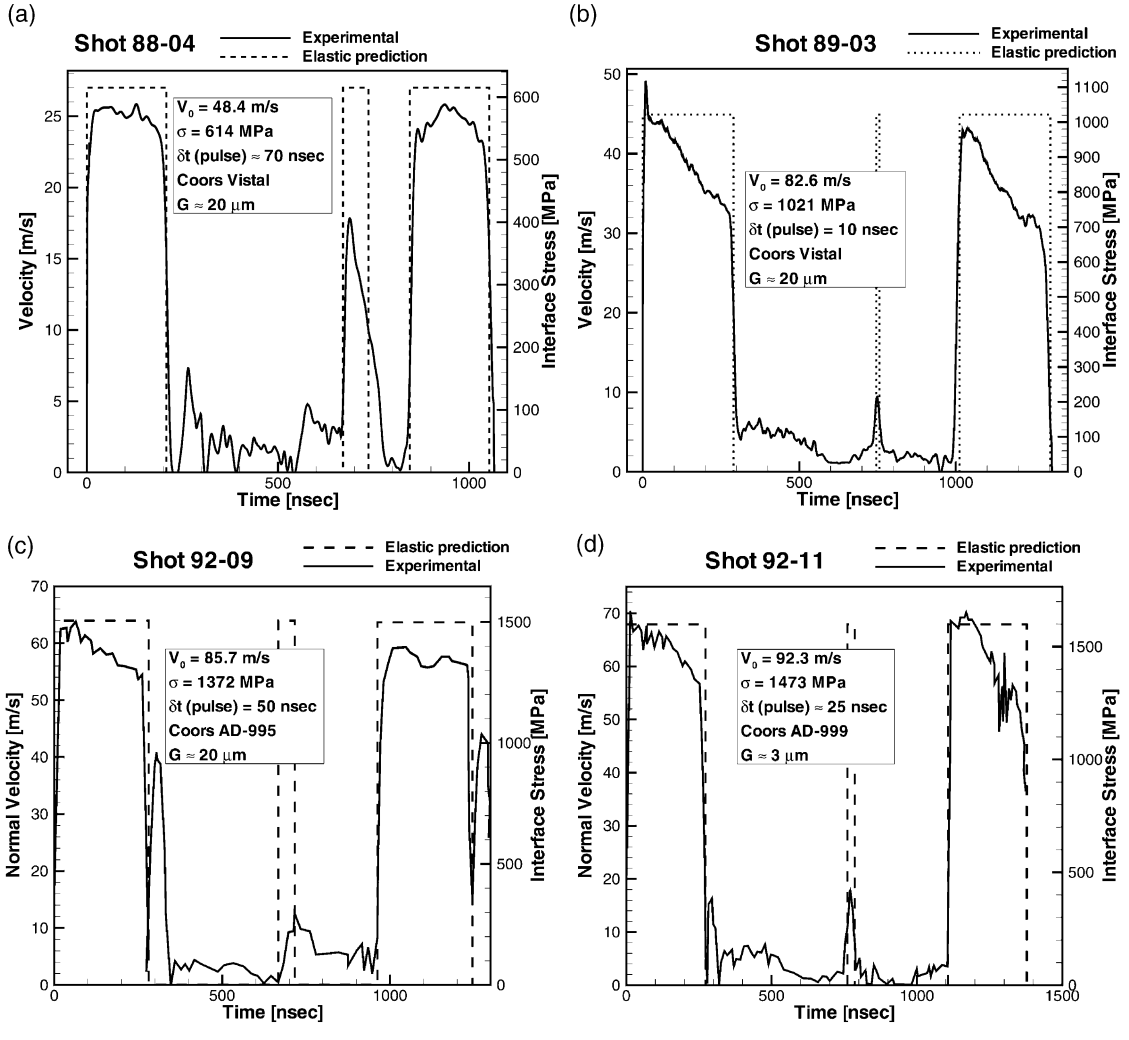

Fig. 3. Experimental particle velocity vs time for different experiments performed by Espinosa *et al*. [4] and Raiser *et al*. [2]: (a) Shot 8804. (b) Shot 8903. (c) Shot 9209. (d) Shot 9211.

For simplification purposes, the nonzero components are denoted by only two indices (i.e. $C_{1111} = C_{11}$, $C_{2222} = C_{22}$, etc). It should be noted that the behavior of the alumina is assumed to be transversely isotropic (or hexagonal), while the real crystal structure is known to be a trigonal system (in which case only one angle can vary). A detailed explanation of why this assumption does not affect the numerical analysis is given in [27].

5. ANALYSIS OF THE SOFT-RECOVERY IMPACT EXPERIMENTS

A first set of simulations using a microstructure with equiaxial grains, shown in Fig. 4(a), and a uniform distribution of grain boundary toughness and strength was performed. It was found that for all experiments and sets of model parameters there is a threshold toughness or strength for which the ceramic develops a set of fast growing microcracks. When K_{IC} or T_{max} was varied, it was observed that the pull-back signal did not change significantly until the transition from intact to fully damaged ceramic was reached.

To circumvent these limitations, two important features were incorporated in the simulation of the experiments, namely,

1. A Weibull distribution of the interfacial strength and fracture toughness along the grain facets.
2. Realistic microstructures considering grain morphology and size distributions.

As discussed in [27, 28, 33], it is physically incorrect to select a uniform T_{max} and K_{IC} for all grain facets. Not only that grain misorientation affects the interfacial strength, but also it affects the presence of glassy phase, glass pockets, and other impurities that modify grain boundary properties. Their random distribution leads to the consideration of a statistical variation in the interfacial strength dependence on grain misorientation and the presence of second

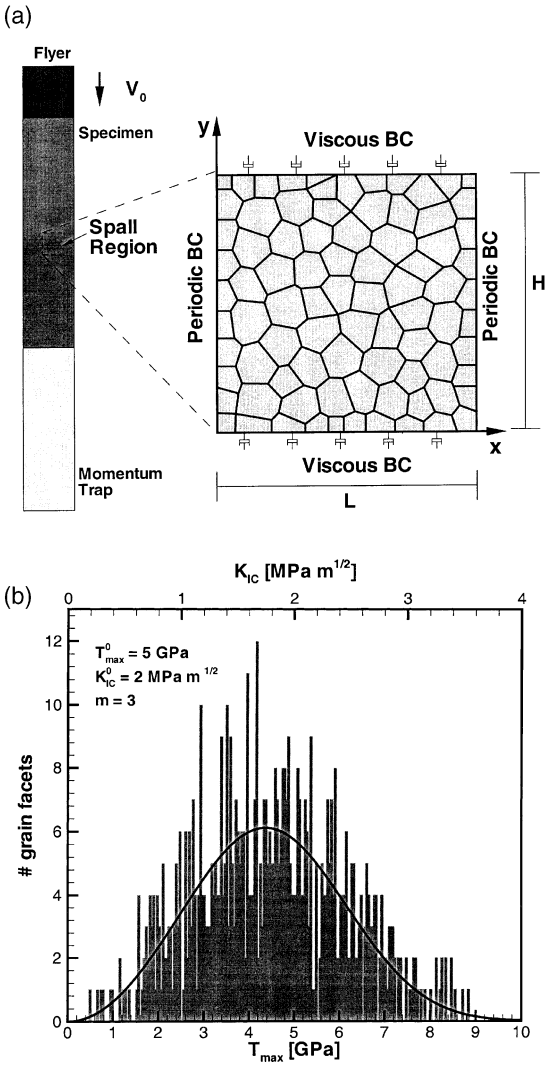

Fig. 4. (a) Schematics of the computational cell used for the analyses. (b) Typical Weibull distribution utilized in these analyses.

phases. In the following analyses, the interfacial strength parameters will be described by a *Weibull* distribution. For instance the weibull distribution for the maximum strength is given by

$$f(T_{\max}) = \frac{m(T_{\max})^{m-1}}{(T^0_{\max})^m}\exp\left[-\left(\frac{T_{\max}}{T^0_{\max}}\right)^m\right],\ T_{\max}>0.$$

A similar expression is used for the Weibull distribution for the fracture toughness. Figure 4(b) shows the histogram for a typical distribution of $T_{\max}$ and K_{IC} used for the simulations presented in these analyses.

5.1. Simulation of experiment 88-04

The impact velocity used in shot 88-04 was $V_0 = 48.4$ m/s and the pulse duration was 70 ns [3–5]. This impact velocity is the lowest examined among all shots. The maximum axial stress is about 614 MPa. Figure 3(a) shows the experimental velocity history for this experiment. The elastic solution is also shown in the same figure. The most significant features of this experiment are the pullback signal (almost 30% of the maximum stress) and the spreading of the second compressive pulse. It is also noteworthy that there is no delay of the pulses.

Numerical simulations using the microstructure shown in Fig. 4(a) result in a pull-back signal with a maximum stress equal to the first compressive pulse, which is well above the pull-back signal measured experimentally. Once microcracks nucleate, they grow at rates such that a major crack from side to side of the RVE develops. It is worth noticing that even for the case in which there is only one nucleation site every 200 μm, the crack has to propagate to the other side of the RVE, in more than 67 ns (tensile pulse duration), in order to have a pullback signal below 100% of the compressive pulse. This would require a crack speed of less than 50% of the Rayleigh wave speed, which for alumina is 3 mm/μs, or a delay in the decohesion process produced by rate effects.

5.1.1. Rate effects. To examine possible failure mechanisms, rate effects are examined in the modeling of grain boundary failure. Rate effects in the interface description can be easily incorporated in terms of the non-dimensional displacement jump λ as given by $T_{\max} = T^0_{\max}(1 + \beta\ln[\dot{\lambda}/\dot{\lambda}_0])$. In this expression, $T_{\max}$ is the maximum interface traction at the current displacement jump rate $\dot{\lambda}$ and $T^0_{\max}$ is the maximum interface traction at a reference displacement jump rate $\dot{\lambda}_0$.

Figure 5 shows several numerical simulations with different values of β. These rate effects seem to be a way to control the pullback signal making it lower for higher values of β. The evolution of the crack length in the entire RVE is also shown in the same figure. Even though this evolution seems to show a lower crack speed for higher values of β, the crack pattern is significantly different, with increasing microcrack diffusion, at higher values of β. It should be noted that although the maximum value of the microcrack accumulated length does not show any marked tendency, the initial slope of the evolution function is governed by β, indicating that the pullback signal is controlled by the rate of the accumulated crack length rather than by the final crack length.

The rate effects make the grain boundary appear stronger when the pulse load is applied. As the wave propagates through the specimen and the zone of the ceramic subjected to tensile stress reaches a steady state, the grain boundary presents an apparent loss of strength as the rate of the displacement jump decreases. Since this steady state is reached after a few nanoseconds upon arrival of the tensile pulse to the spall plane, the region with weaker interfaces becomes broader and microcrack nucleation sites are

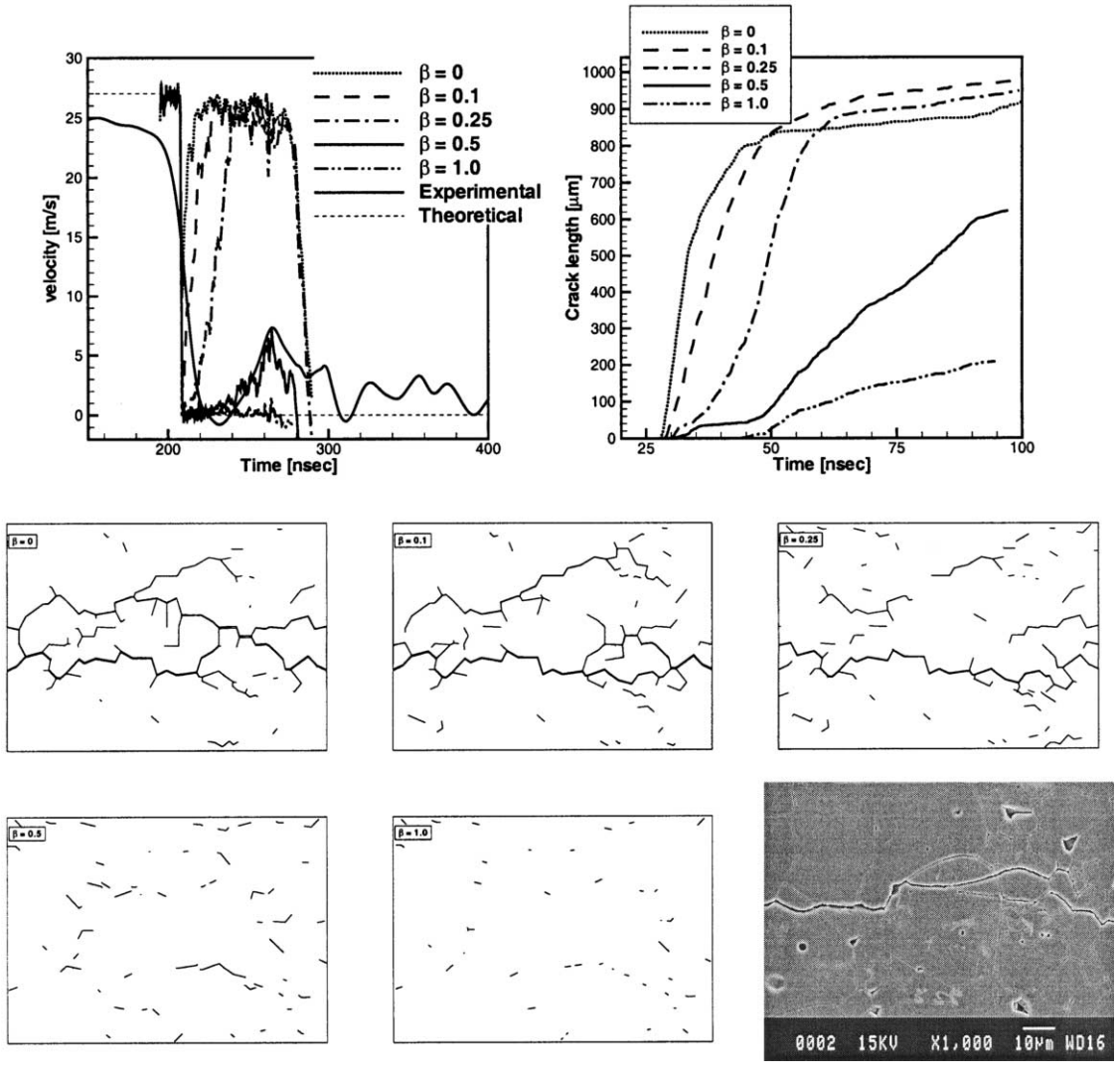

Fig. 5. Rate effects in the numerical calculation of shot 88-04. Several values of β were employed. Even though for the case $\beta = 0.5$ the velocity recorded at the back of the target has a good agreement with the experimental result, the simulated crack patterns show a spread of microcracks rather than a major crack on the spall plane. The last frame is a SEM micrograph of the recovered specimen showing a major crack along grain boundaries and significant crack opening.

spread in all that zone leading to the simulated crack patterns. The dramatic transition in the pullback signal can be explained by the fact that for lower values of β the failure is governed by the initiation of one crack and its propagation through the RVE, rather than the nucleation of several cracks distributed in the same RVE that do not propagate. The transition in which the crack does not propagate along the entire RVE for this particular case occurs at $\beta = 0.25-0.5$. The same observations have been found by authors in other similar analyses [28].

The last frame of Fig. 5 shows an SEM micrograph [5] of the material recovered from shot 88-04. This micrograph does not exhibit the simulated crack pattern corresponding to high values of β, instead a major crack along the spall plane is observed experimentally. In summary, a value of $\beta = 0.5$ can capture the velocity history interferometrically recorded in the experiment but does not produce the crack pattern observed in the recovered specimens. It can be concluded that rate effects are artificial in this type of numerical simulation where the grains are explicitly considered.

5.1.2. Stochastic effects and selection of RVE size. We return our attention to the effect of stochasticity in the strength of grain boundaries. A simulation with the Weibull distribution $T^0_{\max} = 5$ GPa, $K_{IC} = 2$ MPa m$^{1/2}$ and $m = 3$ was performed. The simulation did not show any microcrack initiation in the ceramic microstructure. However, this distribution resulted in spallation when other experiments at higher impact velocity were simulated. A possible explanation for this phenomenon is that the number of grains, and

thus the number of nucleation sites considered in the representative volume element were not large enough to capture *all* possible interfacial strengths as a function of grain orientation and second phases. Hence, nucleation sites could be expected in a larger region than the width used for the assumed RVE. This effect becomes more noticeable when the level of the applied stress is very close to the threshold stress needed to nucleate microcracks. This is the case in experiment 88-04. In fact, the experimental velocity history shows that the second compressive pulse attenuates from a maximum of 600 MPa to 400 MPa (measured threshold stress for spallation).

In the following subsection this feature is examined by increasing the dimension of the RVE to 300 μm and by considering a distribution of grain sizes. Likewise, additional features to be considered are the ceramic average grain size, 20 μm for shot 88-04, and the number of elements needed, inside each grain, to capture the stress concentration at triple points as well as the number of interface elements, along grain boundaries, to capture the crack cohesive zone for high values of $T_{\max}$.

5.1.3. Simulations with more realistic microstructures. A close examination of the many SEM micrographs obtained from several recovered samples [4, 5] provides insight into the path followed by the microcracks during coalescence. It is observed, e.g., in Fig. 5, that the microcracks need to follow grain boundaries, with large variations in grain size. The net effect is that crack propagation speed on a projected horizontal plane is reduced to a fraction of the Rayleigh wave speed. In this section we closely examine this feature in conjunction with the observation of possible nucleation sites as a function of overstress from the threshold level.

Two microstructures are considered in this analysis. Both meshes have a width of 300 μm such that if there is only one nucleation site, the crack will have a total time equal to the pulse duration to coalesce into a main crack. The main idea of this analysis is to compare *vis-à-vis* the crack propagation for two different types of microstructures: Microstructure A, with a non-uniform distribution of grain sizes and shapes (motivated from Fig. 5), and microstructure B with a uniform distribution of grains (all with the same size and similar shape).

Figure 6(a) shows in detail the pullback signal for simulations considering microstructure A. Microstructures A and B are shown in Fig. 7. In these simulations three different Weibull distributions have been considered. The best fit is obtained for a Weibull distribution with $T^0_{\max} = 5$ GPa, $K^0_{\mathrm{IC}} = 2$ MPa·m$^{1/2}$ and $m = 3$. This distribution contains interface elements with $T_{\max} = 0.5$ GPa and $T_{\max} \approx 10$ GPa. The same distributions have been considered for microstructure B, see Fig. 6(b), and the pullback signals are much more pronounced than those obtained with microstructure A. An explanation can be inferred by examining the

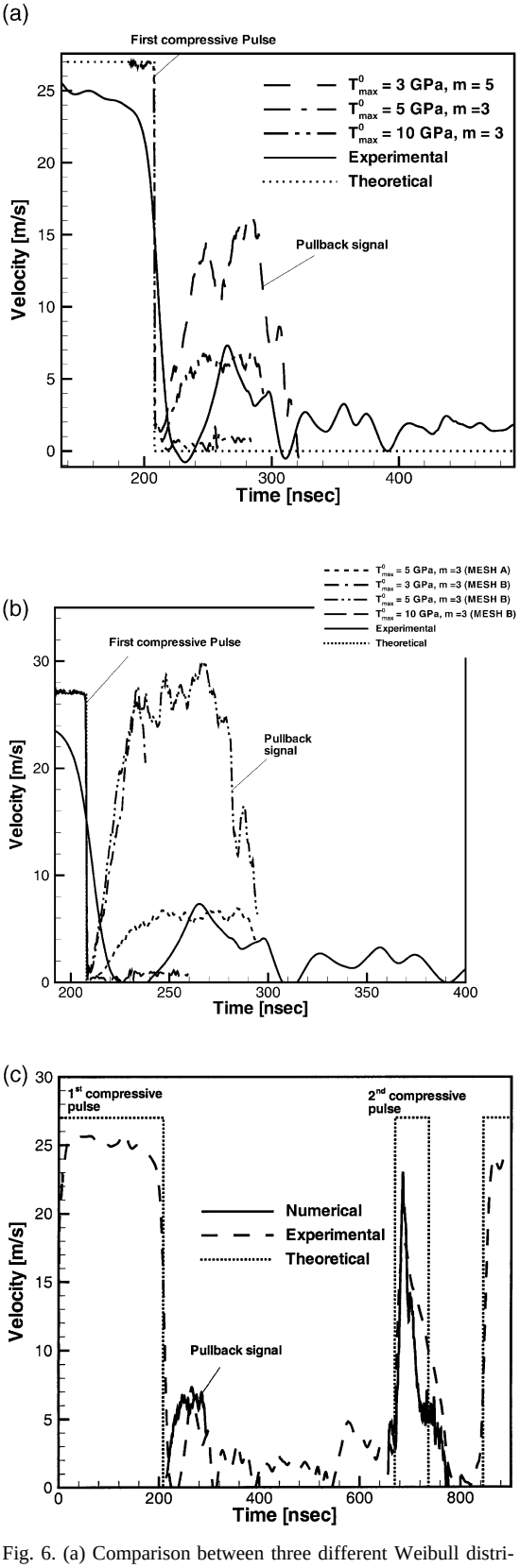

Fig. 6. (a) Comparison between three different Weibull distributions for shot 88-04 using mesh A. (b) Comparison between the velocity history using meshes A and B. (c) Comparison between numerical result, using mesh A, $T^0_{\max} = 5$ GPa, $K_{\mathrm{IC}} = 2$ MPa·m$^{1/2}$, $m = 3$, and experimental data.

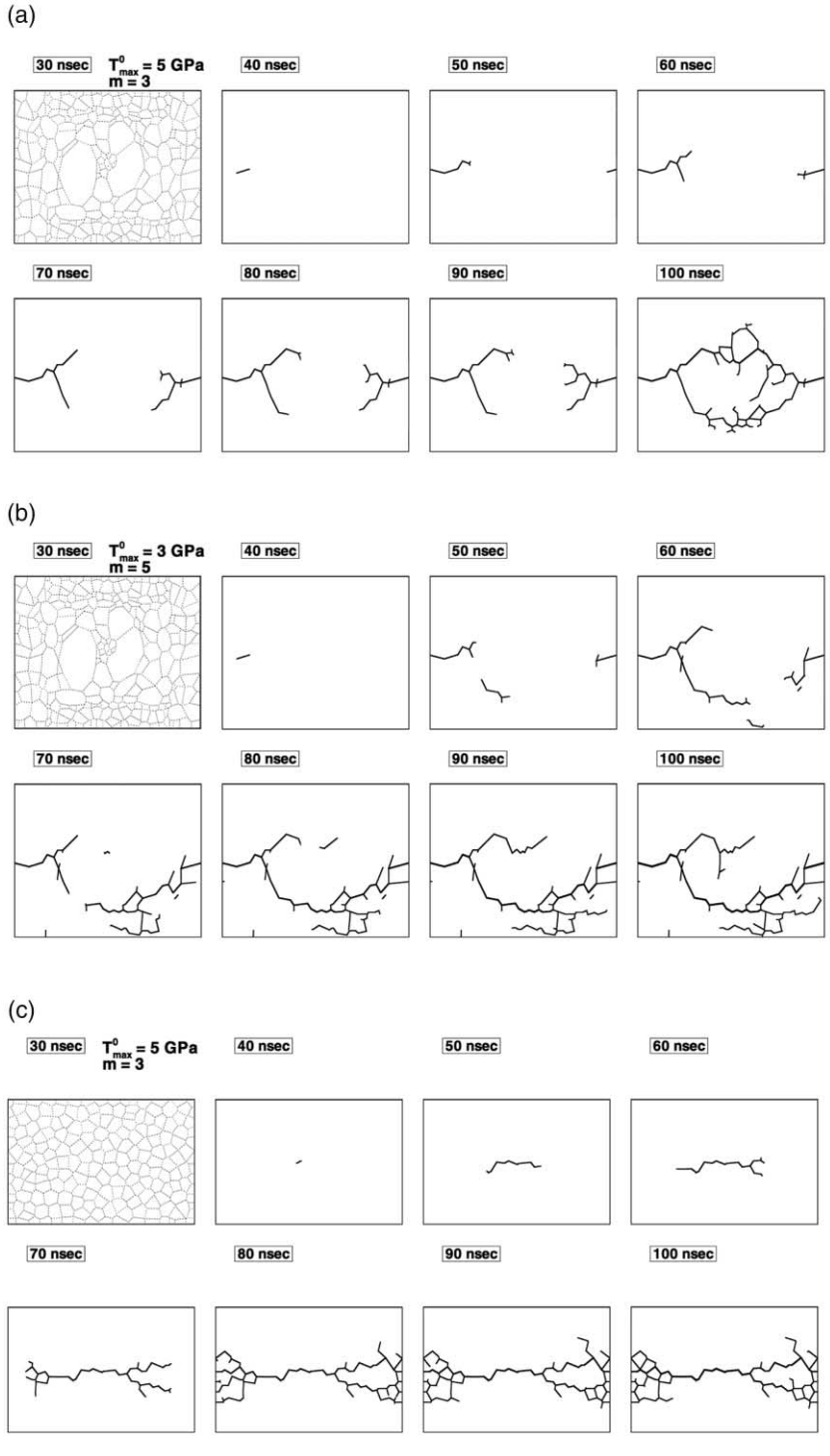

Fig. 7. (a) Evolution of crack pattern for the case with $T^0_{max} = 5$ and $m = 3$ using mesh A. (b) Evolution of crack pattern for the case with $T^0_{max} = 3$ and $m = 5$ using mesh A. (c) Evolution of crack pattern for the case with $T^0_{max} = 5$ and $m = 3$, using mesh B.

evolution of crack patterns as shown in Fig. 7. The evolution of the microcracks for $T^0_{max} = 5$, $K^0_{IC} = 2$ MPa·m$^{1/2}$ and $m = 3$ using mesh A is shown in Fig. 7(a); the grain morphology is shown in the first frame. The same microstructure with a weaker distribution gives another crack pattern evolution (see Fig. 7(b)). In both cases, it can be observed that the microcracks need to go around the large grains at the center of the RVE. The time that it takes the crack to surround the large grains is similar to the pulse duration and then the pullback signal is significantly lower than for cases where the crack propagates, from

one side to the other of the RVE, at uniform speed. Figure 7(c) shows the crack evolution for the case with microstructure B. The crack initiates almost in the middle of the RVE and propagates at constant speed until it coalesces into a main crack just before the tensile pulse vanishes. As a result, the pullback signal for this case is much higher than that for the case where the crack is forced to follow a path around large grains.

Confidence in the model and identified parameters can be obtained only if a variety of impact velocities is examined. In the next and subsequent subsections we address this issue.

5.2. Simulation of experiment 89-03

The impact velocity used in shot 89-03 was $V_0 = 82.6$ m/s and the pulse duration was 10 ns. The first compressive pulse attenuates from 45 to 33 m/s (see Fig. 3(b)). Although the pullback signal is not clearly seen in the experimental trace, it cannot be concluded that in this experiment there is no pullback signal. In fact, due to the attenuation of the compressive pulse, wave spreading occurs masking any short duration pullback signal. The second compressive pulse is attenuated to approximately 20% of its elastic value.

Since the peak tensile stress in this experiment is much higher than the threshold stress for microcracking, the numerical simulation is performed with an RVE of 200 μm×200 μm, average grain size of 20 μm and element size less than 1 μm. SEM observations performed on recovered samples [4] indicate that the grain morphology of the ceramic used for this experiment does not exhibit significant variations in grain size (the Vistal ceramic was purchased from Coors Co. in two batches; shot 88-04 was perfomed on a specimen from the first batch while shot 89-03 was perfomed on a specimen from the second batch). For this reason, a microstructure with relatively uniform distribution of grains has been used. The Weibull parameters used in this numerical simulation for the interfaces are $T^0_{\max} = 5$ GPa, $K^0_{\mathrm{IC}} = 2$ and $m = 3$. For this distribution both $T_{\max}$ and K_{IC} are varied with the same Weibull distribution and seed. A histogram showing the distribution of $T_{\max}$ and K_{IC} as a function of the number of interface elements is shown in Fig. 4(b). For this Weibull distribution, we can see that $T_{\max}$ can vary from 0.5 to about 9 GPa. The theoretical value of this Weibull distribution is plotted in the same figure using a solid line.

Figure 8 shows a comparison between numerical simulation and experimental velocity histories. A good agreement is observed regarding attenuation of the second compressive pulse. The maximum tensile stress as well as the width of the pulse are captured by the simulation. After the first compressive pulse, the simulation presents a pullback signal with the maximum stress equal to 40% of the maximum compressive stress. A larger distribution in grain size than employed in the simulation may explain the reduced pull-back signal experimentally recorded. Likewise, as a result of the small but finite tilt between ceramic and anvil plates, as well as the dispersion of the first compressive pulse, the short pullback signal may be slightly hidden in the experimental trace.

Since the focus of this investigation is to gain insight into tensile failure in brittle materials, the compressive wave attenuation associated with grain boundary shearing [4, 5], not capture by the numerical simulation, is postponed to a later section. The spreading of the first compressive pulse and the effect of spherical waves emanating from the corners of the star-shaped flyer contribute to the non-zero velocity between first and second compressive pulses. In view of the fact that our 2-D model does not include these effects, the tail following the first compressive pulse is not present in the computed normal velocity history.

A study of the effect of grain size has been performed for this experiment using the identified parameters. Figure 9 shows the velocity histories for two microstructures with an average grain size of 2 μm and 20 μm, respectively. The simulation corresponding to a microstructure with an average grain size of 2 μm exhibits very little damage and absence of pullback signal. This feature is quite interesting. Figure 10 shows the distribution of σ_{yy} along a horizontal line at 1/4 from the top of the RVE. An interesting observation is that the stress concentration corresponding to an average grain size of 2 μm is larger than for the case with an average grain size of 20 μm. However the overall stress level is much lower in the case of the smaller average grain size making difficult the propagation of the microcracks initiated due to the stress concentration.

5.3. Simulation of experiment 92-09

In this subsection we examine an experiment with similar impact velocity as shot 89-03 but with a pulse duration about five times larger. The impact velocity for shot 92-09 was $V_0 = 85.7$ m/s and the pulse duration was 50 ns. The most noteworthy feature of the experimental velocity history is the pullback signal of about 60% of the compressive pulse (see Fig. 3(c)). The second difference that must be taken into account is that this experiment was performed with another type of alumina, in this case Coors AD-995 instead of Coors AD-999 or Vistal. The larger glass content is simulated by varying the Weibull distribution. It is reasonable to assume that the specimen contains a larger number of grain boundaries with low strength, in other words, low values of $T_{\max}$.

The same $T^0_{\max}$ of 5 GPa, used for experiment 88-04, has been examined with a lower Weibull parameter ($m = 1$). Although lower values of m tend to spread the values of $T^0_{\max}$, it did not produce the expected outcome. For that reason, both parameters, m and $T^0_{\max}$ have been varied. Figure 11 shows the velocity at the back of the momentum trap for the Weibull distributions with $T^0_{\max} = 3$ GPa, $K^0_{\mathrm{IC}} = 2$ and

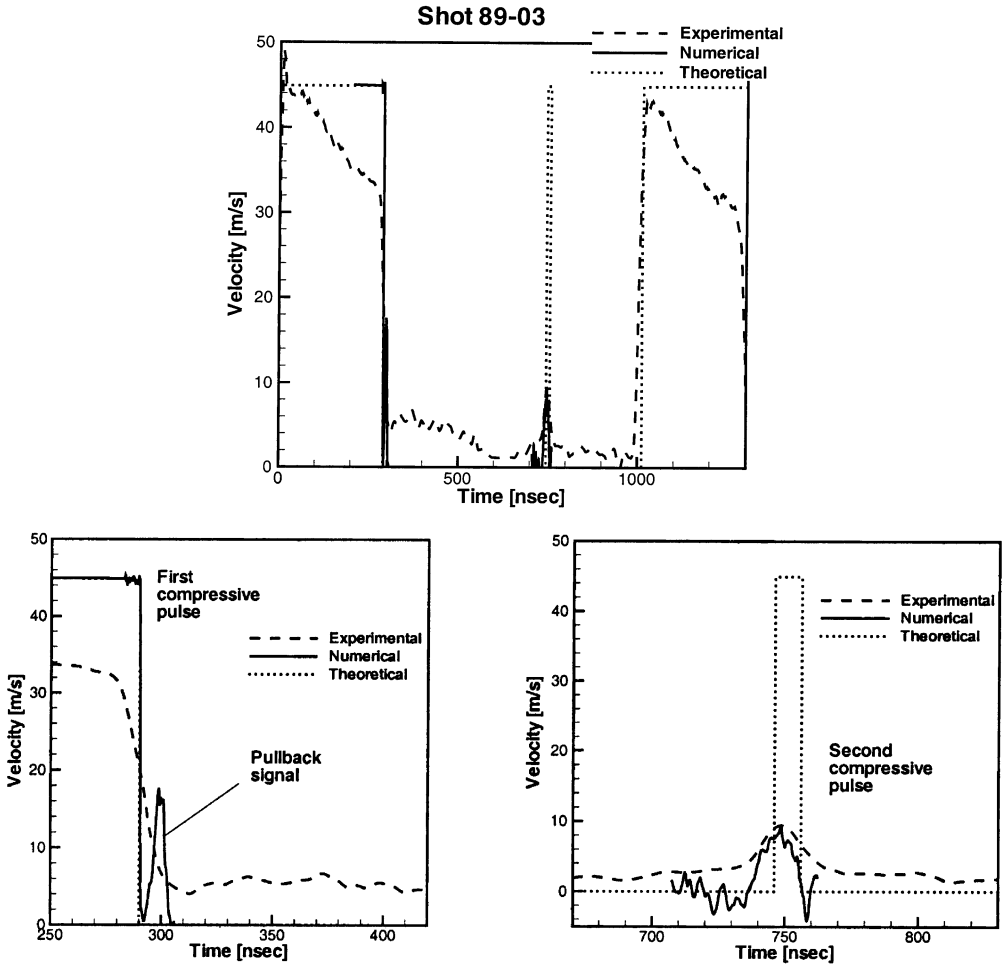

Fig. 8. Comparison between the numerical simulation and experiment for shot 8903.

two different Weibull parameters, $m = 3$, and $m = 5$. The mesh utilized in this analysis is mesh A also utilized in the analysis of shot 88-04. The detail of the pullback signal shows that the best match is obtained with $m = 5$. The distribution with $m = 3$ seems to be much weaker and does not capture the appropriate damage kinetics of the ceramic.

Figure 12 shows the crack pattern evolution for both cases. It can be observed that for the weaker case ($m = 3$), the microcracks propagate faster and the large grains do not significantly delay the microcrack. Instead, the microcracks find another path where the grain boundaries are weaker (at the bottom of the RVE) and concentrate in the region with smaller grains as opposed to the experimental observations. For the case with $m = 5$, another phenomenon happens, at the time where the microcracks reach the large grains, the microcracks are not only delayed but also new nucleation sites appear in the neighborhood of the large grains as the tensile pulse is held (see Fig. 12(b)). The duration of the tensile pulse to allow these new microcracks to propagate and coalesce, along the RVE, is not long enough. This effect is reflected in a pullback signal with peak particle velocity of 50 m/s.

5.4. Simulation of experiment 92-11

The impact velocity used in experiment 92-11 was $V_0 = 92.3$ m/s and the tensile pulse duration was 25 ns. The main variation in this experiment is the average grain size of the ceramic, Coors AD-999, of approximately 3 μm. For this analysis an RVE of 200×200 μm is considered and two type of microstructures, uniform and bi-modal grain sizes, are analyzed. The main motivation for examining two different microstructures is to study the effect of grain morphology and how this affects the crack path and crack speed along the spall plane. Although the second microstructure with a bi-modal distribution of grain sizes may not be totally representative of the tested ceramic, it is used to evidence the effect of grain morphology.

An analysis with three different Weibull distributions on the RVE with uniform grain size has been carried out; weak interface case: $T^0_{\max} = 3$ GPa and $m = 3$; the case considered in previous experiments,

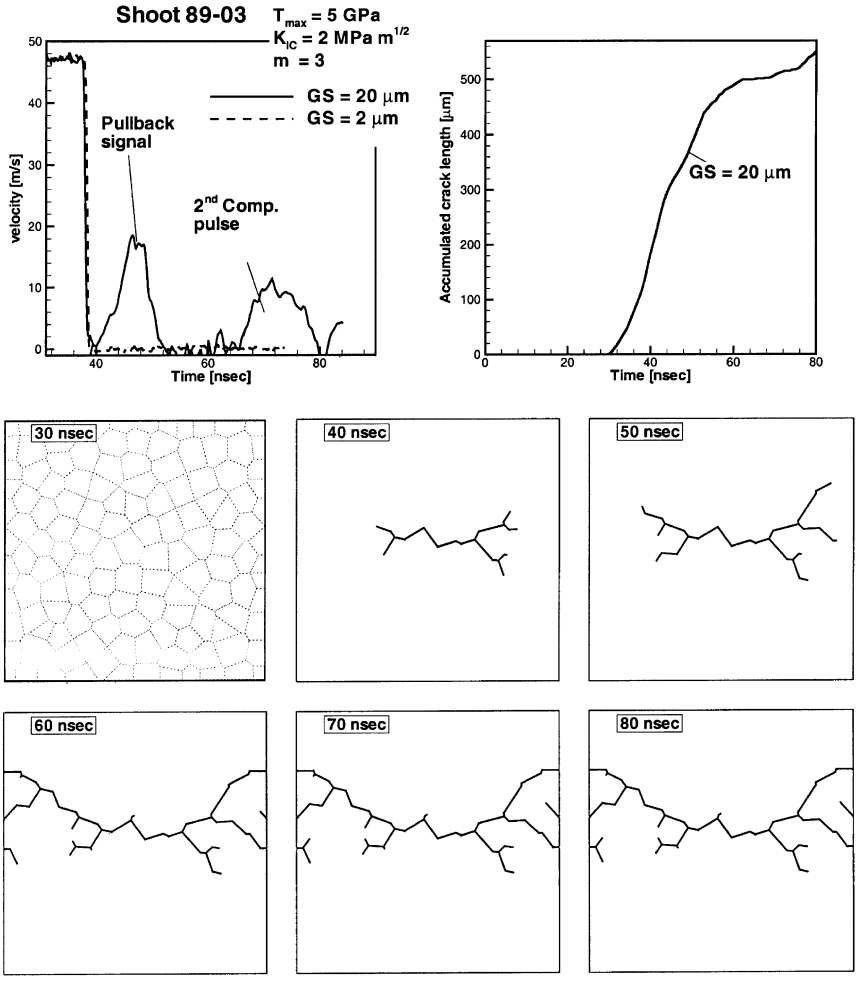

Fig. 9. Velocity history for the numerical simulation of shot 8903 with two grain sizes. The crack length evolution is only shown for the case with grain size 20 μm. The second compressive pulse is shifted in time for plotting purposes. The microcrack evolution showing crack nucleation, growth and coalescence for the case with average grain size of 20 μm is also included in this figure.

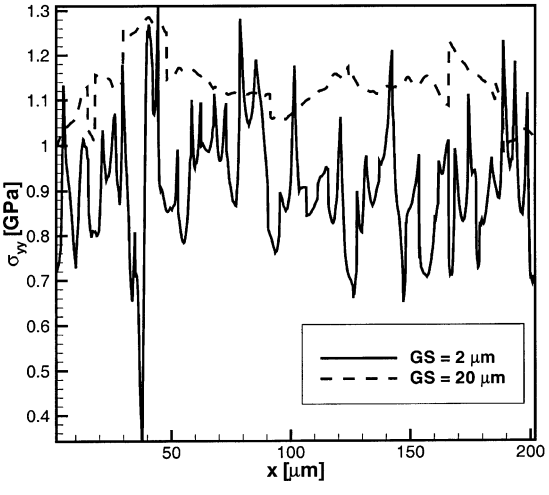

Fig. 10. σ_{yy} vs. x at 1/4 from the top of the RVE for two different average grain sizes.

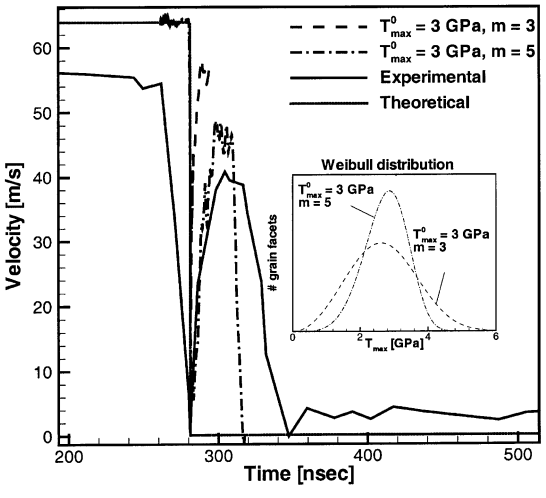

Fig. 11. Velocity history for shot 9209 as a function of Weibull distributions.

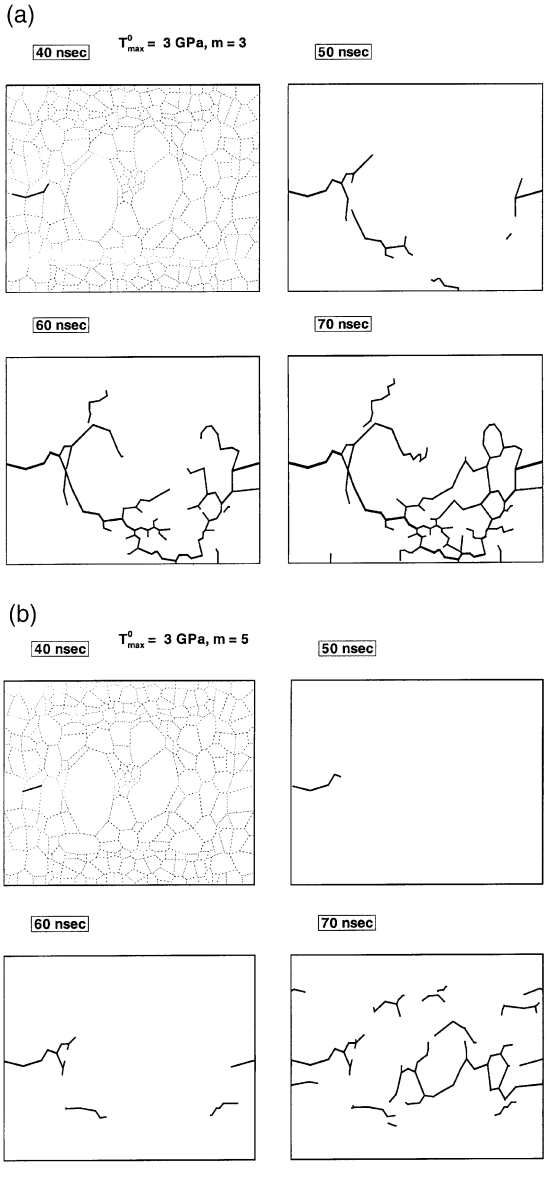

Fig. 12. Crack evolutions for two Weibull distributions: (a) $T^0_{max} = 3$, $K_{IC} = 2$ MPa·m$^{1/2}$ and $m = 3$. (b) $T^0_{max} = 3$, $K_{IC} = 2$ MPa·m$^{1/2}$ and $m = 5$.

i.e., $T^0_{max} = 5$ GPa and $m = 3$; and a strong interface case: $T^0_{max} = 10$ GPa and $m = 10$. The intention of this analysis is not to study parametrically the effect of m, or T_{max}. It has been observed previously [28], that a study of the different Weibull parameters does not add any valuable insight into the problem. Instead, we decided to present three extreme cases. The idea is to see the effect of the distribution (not each individual parameter) on the capability of the material to absorb energy in the form of crack branching.

In all cases $K_{IC} = 2$ MPa·m$^{1/2}$. Figure 13 shows the crack pattern for each one of these cases; the grain morphology is shown in the first frame. In the weak interface case, the ceramic fails from side to side right after the tensile pulse is generated at the spall plane. Crack nucleation occurs basically at a large percentage of triple points and coalescence of microcracks occurs before the end of the tensile pulse. For the case with $T^0_{max} = 5$ GPa and $m = 3$ the crack start propagating from the center to the borders and crack branching in the form of a *funnel* is observed. As expected, the strongest case ($T^0_{max} = 10$ GPa and $m = 10$) shows less branching and microcrack density. The energy to create new surfaces is higher so that branching is inhibited.

The pullback signal for these three cases is plotted in Fig. 14. The weak interface case $T^0_{max} = 3$ GPa and $m = 3$ results in a large pullback signal and full unloading of the first compressive pulse does not occur. The particle velocity drops to about 40 m/s and then sharply rises to 72 m/s. The rise time is extremely small. The other two cases present a smaller rise time and the peak velocities do not reach 72 m/s. The case with more branching ($T^0_{max} = 5$ GPa and $m = 3$) results in a higher pullback peak velocity than in the case of strong interfaces, i.e., $T^0_{max} = 10$ GPa and $m = 10$.

The same analysis has been carried out for the microstructure with a bi-modal distribution of grain size and shape. The Weibull distributions are the same, except that the weakest case has not been considered and a new case with $T_{max} = 10$ GPa = constant has been included. The pullback signal for these cases is shown in Fig. 15(a) while the attenuation of the second pulse is shown in Fig. 15(b). The pullback signal and second compressive pulse for the strongest case ($T_{max} = 10$ GPa = constant), is not in good agreement with the experiment, stressing once more the fact that distributions in strength and toughness are characteristic features of the tested ceramic microstructures. Only the cases with $T^0_{max} = 5$ and 10 GPa and Weibull distributions have a similar second compressive pulse. The pullback signal is overpredicted at early times implying that more microstructural details are needed. Unfortunately, the paper by Raiser *et al.* [2] did not provide SEM images of the recovered specimen.

The crack pattern for these cases is plotted in Fig. 16(a) and (b), respectively. Here, the same phenomenon observed for shot 88-04 can be appreciated. The cracks are temporarily delayed when they reach the elongated grains and spend additional time surrounding them. The phenomenon is repeated in all three cases, except that the crack speed, along the spall plane, is reduced for the cases with stronger interfaces.

5.5. *Damage in compression*

Examination of the experimental results, shots 89-03, 92-09 and 92-11, clearly show attenuation of the first compressive pulse. Espinosa [5] has shown that this inelasticity results from grain boundary shearing rather than microcracking in compression. The source of such shearing is associated with the presence of thin glass films, a few nanometers in thickness [5].

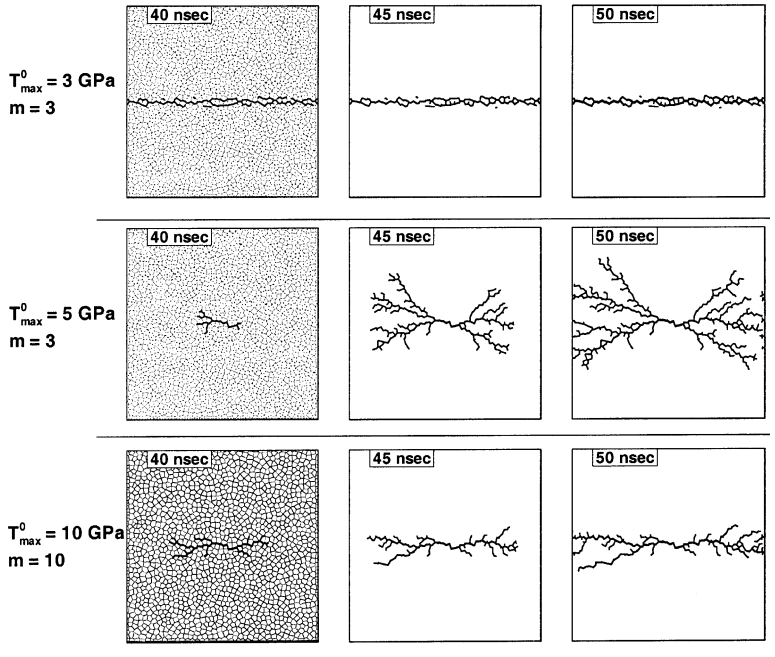

Fig. 13. Crack pattern evolution for shot 9211 using a microstructure with a uniform distribution of grain size and three different Weibull distributions.

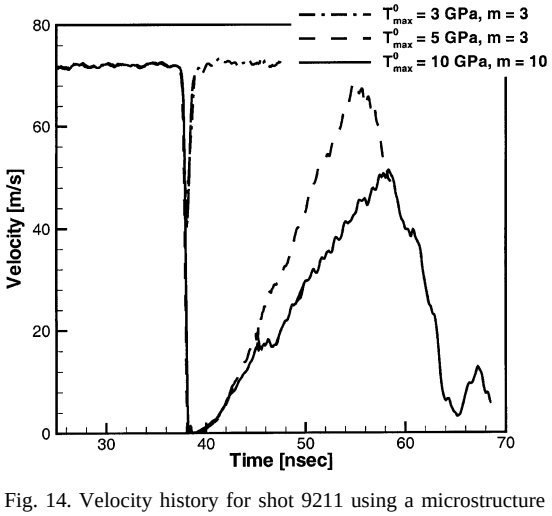

Fig. 14. Velocity history for shot 9211 using a microstructure with a uniform distribution of grain size and three different Weibull distributions.

These glass films have the effect of reducing the shear resistance of the grain boundaries. A sudden drop in glass shear resistance, upon accumulation of shear deformation, was first observed by Espinosa [5] and later further investigated by Clifton and Sundaran [35] using pressure–shear experiments. They found that when the shear strain in glass reaches about 200% a sudden drop in shear resistance occurs.

We next present an analysis of inelasticity in compression taking into account these features. For these simulations, the representative volume element of Fig. 17 is utilized. In the same figure, it can be observed that glassy phase and glass pockets have been included following TEM observations [5]. Once again, because of the number of elements needed in the simulation, a small RVE is considered rather than the whole thickness of the specimen. Therefore, the simulation can provide only the trends of the phenomenon rather than a detailed quantification of compressive pulse attenuation. The material parameters for the glass are given in Table 1. The finite deformation visco-plasticity model presented in Espinosa *et al.* [30] is used to model the glass pockets.

The amount of glass included in the model has been calculated for the ceramic Coors Vistal with Al_2O_3 wt% of 99.9, which means that $(\rho_{glass}V_{glass})/(\rho_{glass}V_{glass} + \rho_{alu}V_{alu}) = 0.001$ where V_{glass} is the volume of the glass, V_{alu} the volume of the alumina and $V_t = V_{glass} + V_{alu}$. This leads to the relationship between the volume of glass and total volume as $V_{glass} = 0.001V_t$. For $\rho_{glass} = 3550$ kg/m^3 and $\rho_{alu} = 3990$, and considering a glass pocket between 1–2 μm^2, for the RVE shown in Fig. 17, the number of glass pockets is about ten. It is also assumed that interfaces contain glassy phase only if they are connected to glass pockets. This assumption is based on thermodynamical arguments and TEM observations [5].

The interfacial parameters for the glassy phase have been obtained considering the fact that the glass yields at a shear stress of about 500 MPa and loses shear strength when the shear strain reaches $\gamma = 200\%$. Using the cohesive law III described in Espinosa *et al.* [31] and improved in Zavattieri and Espinosa [28], a $\tau_{max} = 500$ MPa and $\delta_t = 0.2$ μm, for a glass layer thickness of 100 nm, the interface

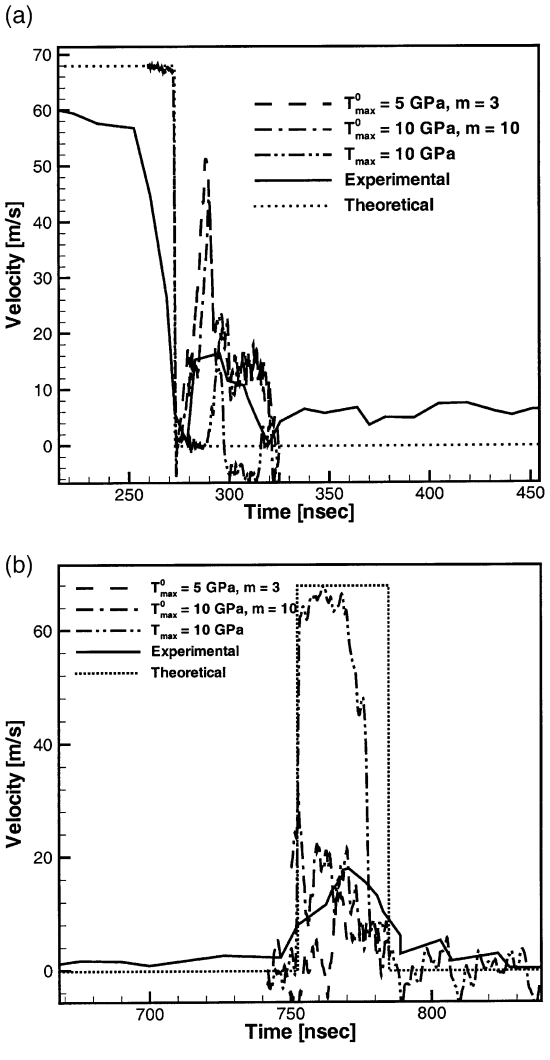

Fig. 15. Velocity history at the back of the momentum trap, using a mesh with a bi-modal distribution of grain sizes.

behavior can be captured. Glassy phase is considered only on grain facets connected to glass pocket. The rest of the facets are simulated with a Weibull distribution of $T^0_{max} = 5$ GPa, $K^0_{IC} = 2$ and $m = 3$.

Experiment 89-03 is re-examined due to the experimentally observed strong velocity attenuation of the first compressive pulse, which clearly shows the presence of relaxation under a fully compressive stress state. Figure 18(a) shows the computed velocity history at the back of the momentum trap. Although this simulation shows qualitatively the same attenuation observed in the experiments, it cannot quantitatively be compared with the experiments due to the fact that only a portion of the total thickness of the ceramic has been considered. The attenuation achieved in this simulation is approximately 0.8 m/s along 120 μm. If the real thickness of the specimen, about 4 mm, is considered for the RVE an attenuation of approximately 24 m/s would be expected. The experimentally observed attenuation is about 16 m/s. The numerical overprediction is not surprising if one takes into account that the model is 2-D and that the exact distribution of glass within the microstructure is difficult to assess. However, a progressive decay in velocity is properly captured!

The crack pattern as a function of time is also shown in Fig. 18(b). Microcracks emanating from the glass pockets are produced. It should be mentioned that the presence of glass pocket has been essential for inducing microcracking. Simulations with glassy phase in the form of thin films and no glass pockets did not present any microcracking. The compressibility and inelasticity of the glass pockets is believed to provide the grain shearing deformation needed to induce microcracking, along grain facets, under a stress state with all compressive principal stresses.

The same representative volume element has been used to simulate spallation. Two cases are compared, the microstructure with the ceramic already damaged by the compressive wave and without damage. Figure 19 shows the resulting pullback signal simulated at the back of the momentum trap for both cases. This analysis shows that damage in compression does not have a significant effect in subsequent ceramic microcracking under tension. This finding is consistent with the velocity histories and microscopic observations performed on recovered specimens [4, 5].

5.6. *Effect of residual thermal stresses*

Quasi-static simulation of the residual thermal stresses during cooling in the sintering process, have been performed by Zavattieri and Espinosa [28]. In this section we briefly comment on the effect of thermal residual stresses on the dynamic response of the material. Several simulations with different Weibull distribution have been examined with and without the effect of thermal stresses. The temperature drop considered in the analysis was $\Delta T = 1500$ K. An RVE with a cohesive law describing the bonding between grains together with thermal and elastic anisotropy was also considered [28]. Nonlinearities arising from microcracking and glass pocket deformations as a function of temperature were taken into account in the prediction of thermal residual stresses within the microstructure.

No noticable effect on the tensile failure of the material has been found when the RVE includes thermal residual stresses. Whether or not microcracking is more significant in some cases could not be established unambiguously with the assumed stochasticity. One possible reason is the size scale in which the the analysis is being performed. The effect of residual thermal stresses in small representative volume elements affects the stochastic nature of the phenomenon. A larger number of manifestations and a much larger representative volume element (i.e., 1000×1000 μm) appears to be required. Improvements in software and hardware may make such calculations feasible. Nonetheless, our calculations reveal residual thermal stresses of the order of a few

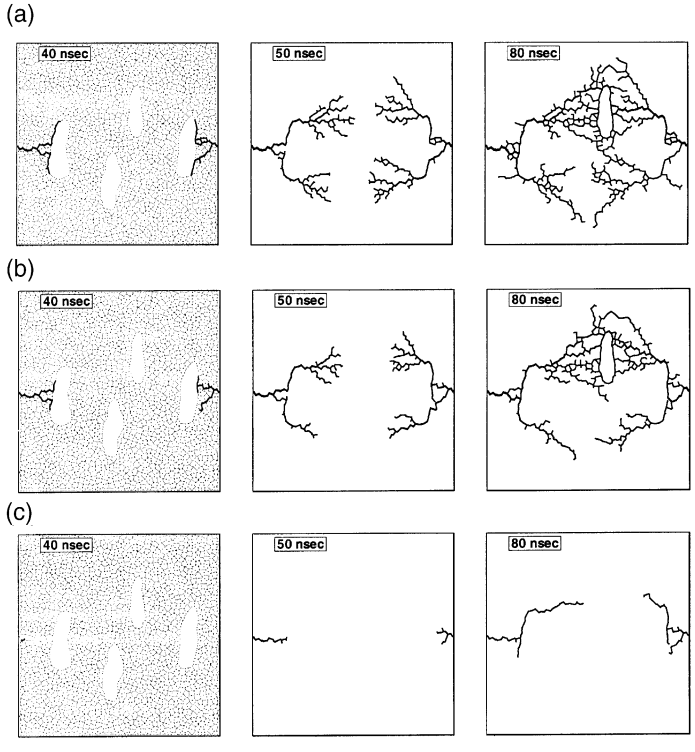

Fig. 16. (a) Microcrack pattern for the case with a microstructure with a bi-modal distribution of grain sizes and T^0_{max} = 5 GPa, K_{IC} = 2 MPa·m$^{1/2}$ and m = 3. (b) Microcrack pattern for the case with a microstructure with a bi-modal distribution of grain sizes and T^0_{max} = 10 GPa, K_{IC} = 2 MPa·m$^{1/2}$ and m = 10. (c) Microcrack pattern for the case with a microstructure with a bi-modal distribution of grain sizes and T_{max} = 10 GPa = constant.

MPa in the case of a microstructure with an average grain size of 20 μm. Such a stress level is well below the applied macroscopic stress in the examined experiments and consequently a minor role in determining microcrack initiation sites and stress thresholds can be expected. A more significant effect of thermal residual stresses could be on the development of frictional tractions that typically develop in grain bridging of cracks having a length of several times the average grain size. This is likely another controlling factor of microcrack propagation speed and by implication pull-back signal.

6. CONCLUDING REMARKS

In this paper, a micromechanical model has been used to simulate normal plate impact *soft-recovery* experiments some of which were performed more than 12 years ago. The experimentally observed damage in compression in ceramics containing second phases, at stress levels well below the dynamic compressive yield stress under uniaxial strain, remained a controversial issue. Likewise, the coupling between compressive and tensile damage was not fully explained as a function of material microstructure. Hence, identification of damage modes experimentally observed in tension and compression awaited the development of unique computational tools and multiprocessor machines with the capability to handle large scale computations. Here we presented a first of its kind grain level investigation of the phenomenon.

Our numerical results are interpreted in terms of microcrack patterns, evolution of crack density, and free velocity histories. Examining all features simultaneously is essential to draw meaningful physical conclusions. A previous parametric study performed by the authors [28] shows that the cohesive interface parameters T_{max} and K_{IC} and their distributions control damage initiation and kinetics. For instance, K_{IC} controls crack propagation rate and the pullback signal tends to disappear as K_{IC} is increased. T_{max} is a threshold parameter that controls crack nucleation. When T_{max} is above a threshold value, damage does not initiate. The value of T_{max} and its *distribution* determines the spall strength of ceramics. An interesting feature proved in our studies is that at the size scale, at which these analyses are considered, there are no rate effects! Unlike other numerical analyses performed on ductile materials and where the RVE employed in the analyses has other dimensions [36], these simulations show that, although rate effects help to match the experimental velocity histories, the microcrack patterns are not in agreement with SEM observations performed on recovered specimens.

The micromechanical analyses, together with the experimental velocity profiles and SEM observations, have demonstrated that there are two factors to be taken into account to capture the right damage kin-

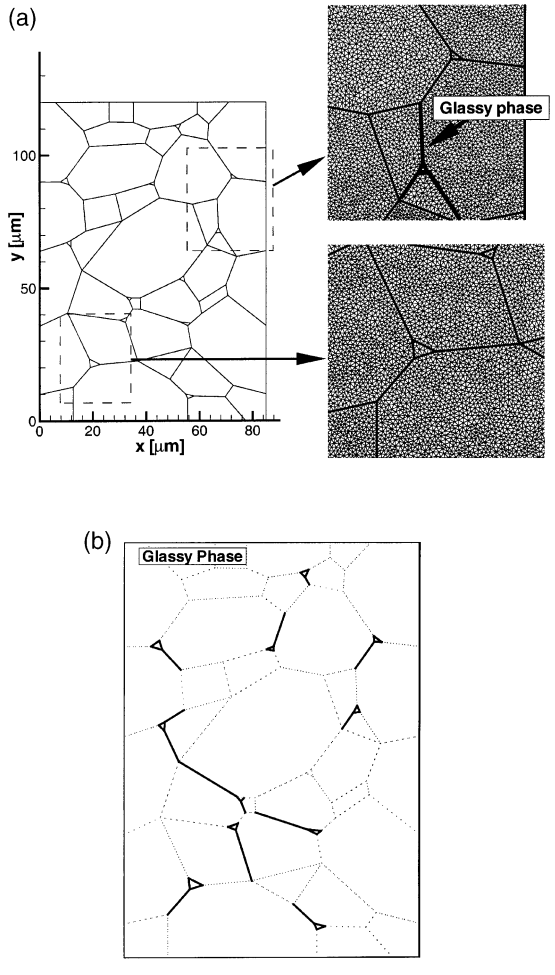

Fig. 17. (a) RVE and mesh utilized to study damage in compression. (b) Detail of glassy pocket and emanating thin glassy films along facets.

Table 1. Material parameters for glass

Elastic	Inelastic
Young's modulus $E = 101.2$ GPa	Initial yield stress $\sigma_0 = 0.75$ GPa
$\nu = 0.264$	Reference plastic strain $\epsilon_0^p = 0.00741$
$\rho = 3550$ kg/m^3	Reference plastic strain rate $\dot{\epsilon}_0^p = 1000$ s^{-1}
$\lambda = 44.78$ GPa	Rate sensitivity exponent $\alpha = 5$
$\mu = 40.03$ GPa	Hardening exponent $\beta = 5$

etics occurring during the experiments. In view of the fact that not all grain facets have the same interface strength and local fracture toughness, it is important to consider Weibull distributions of $T_{\max}$ and K_{IC}. Similarly, since the ceramic microstructures interrogated in these experiments do not contain grains with the same shape and size, microstructures with non-uniform distributions of grain size and shape must be considered. The first feature is not only necessary to capture the right crack speed in the material, but also introduces a simplification in the model. Instead of

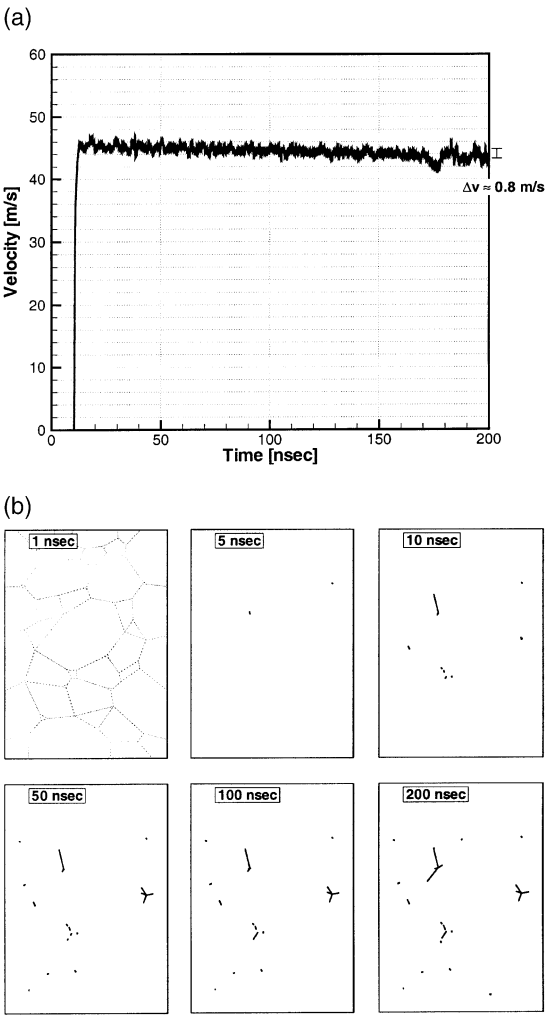

Fig. 18. (a) Velocity history of first compressive pulse, at the back of the momentum trap, for the first 200 ns. (b) Crack pattern resulting from grain boundary shearing and local tensile stresses in a macroscopic stress state with all three principal stresses being compressive.

considering explicitly grain facets with glassy phase, pores, glass pockets, etc., only three parameters are needed to simulate the microstructure: $T^0_{\max}$, K^0_{IC} and m. Besides, data on grain boundary toughness and strength as a function crystal misorientation, chemical impurities and presence of glassy phase is very limited and incomplete in the literature.

On the other hand, microstructures with non-uniform distribution of grain size and shape strongly affect crack speed along the spall plane. When a microcrack encounters grains with a size above the average grain size, it needs to surround these grains in order to continue with the path along maximum macroscopic tensile stress. As a result, the *effective* crack speed, which is the projected crack speed along the spall plane is strongly affected by this effect. The more time the crack has to spend surrounding large grains, the smaller the effective crack speed is. Similar conclusions have been obtained by Xu and

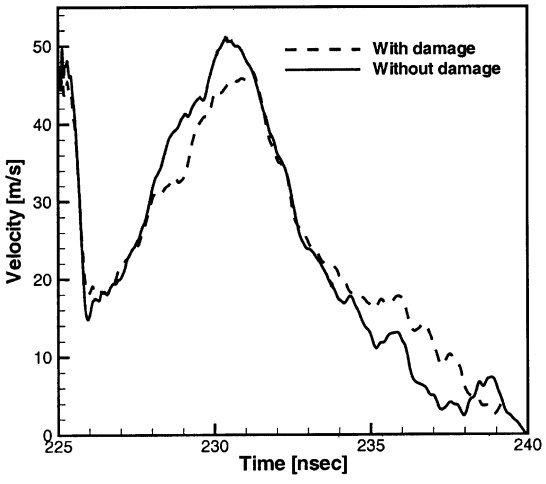

Fig. 19. Pull-back velocity history at the back of the momentum trap for both with damage in compression and without compressive damage.

Needleman [17, 37] although their analysis was not carried out at the grain level.

It should be mentioned that, in this work, the distribution of the interfacial strength is totally independent of the grain size, shape or orientation. Hence, the crack nucleation should not necessarily be given by the grain size. Regardless of whether or not the RVE is shifted half period to the left, the initiation site will not depend on the grain size and location of the grains, instead it will depend on the Weibull distribution of the interfacial strength and the particular seed used in its generation. For a RVE with a uniform distribution of grains, the initiation site does not have any effect on the results reported here. Any crack that goes out to the right of the RVE comes in on the left of the RVE. For instance, in the analyses shown in Fig. 13 the same results would be obtained if the crack initiates in the border of the RVE. If the crack initiates on the boundary of the large grain, it will equally have to propagate around it and as a result the projected velocity in the spall plane will be a fraction of the Rayleigh wave speed. Furthermore, here we do not intend to cover all the possible scenarios corresponding to the location of crack initiation other than what is obtained from the Weibull distribution based on a particular seed. Many more manifestations could be obtained by changing the seed which would result in other crack nucleation sites. Likewise, the location of the first microcrack in the RVE may be affected by the state of residual stress in the microstructure. In [33], the residual stress state, resulting from the manufacturing of the ceramic, was simulated for the same RVE. Values of stress between 20–120 MPa were obtained along grain boundaries with peak stresses at triple points. However, in view of the fact that the applied dynamic stress is about one order of magnitude higher, no significant effects were observed. It is likely that the superposition of residual stresses and dynamically applied stresses may lead to crack initiation at the boundary of the largest grains. This feature will be examined in future work. It is important to note that the findings reported in this paper, in relation to the macroscopic response of the material, would not be changed by the location of the first microcrack within the RVE. It is known that when the loading is highly dynamic, multiple microcracks can nucleate within the material because stress relaxation, due to damage, is not instantaneous. This is clearly in contrast to the case of quasi-static loading.

In this work the effect of grain size has been also studied; Fig. 9 shows this effect. The microstructure with smaller average grain size was stronger than the one with larger grains. The distribution of stress along a horizontal line through the RVE shows higher values of stress at the grain boundaries for the cases with larger average grain size. Additional studies should be performed based on the presented micromechanical model to further examine the physical reasons behind this phenomenon.

Wave attenuation due to inelasticity in compression has also been captured. The key feature included in the model is the presence of glassy phase as thin films along grain boundaries and glassy pockets. Several simulations without glassy phase has been performed in the past without success. Regardless of the maximum strength of the grain boundaries, if the grains do not have the freedom to rotate and translate, microcracking cannot occur. The presence of glass pockets at triple grain junctions allows the needed deformability for grains to slide and rotate, resulting in nucleation of short microcracks along the grain facets. The glassy phases between grains have been simulated using a *hybrid* cohesive interface element, our law III, where the tangential traction is governed by a cohesive law that allows the shear deformation of the glass. The cohesive law includes the coupling between normal and shear deformations [28, 31].

From a computational standpoint, simulations of ballistic penetration, vehicle crash analysis, manufacturing processes, etc. cannot be conducted at the grain level. Hence, this fundamental study of brittle failure provides insight into the utilization of cohesive laws at other size scales. Our simulations clearly show that the scale at which simulations are performed plays an important role in the selection of cohesive models. Not only cohesive interface parameters (T_{max} and K_{IC}) may be different at larger scales, but also the cohesive law *per se*. While at the grain level the cohesive interface element represents the cohesive separation between grains, a simulation of crack growth at larger scales should take into account all the microstructural effects revealed in this study. For instance, microcrack speed should be in accordance with the grain morphology and size in order to account for the time that microcracks take to surround large or elongated grains. This in turns implies a limiting crack speed of about 0.3 the Rayleigh wave speed in the material. Microstructures containing sev-

eral phases may also modify the macroscopic behavior in counterintuitive ways.

The calculations in this work make assumptions that limited the degree of achievable accuracy. For instance, the model is 2-D. As a result, a true random orientation of grains cannot be modeled in the representative volume element. In fact, in each grain, one of the principal axes must always coincide with the global z axis. Moreover, crack interaction is stronger than in the 3-D case and therefore, the computed rate of crack coalescence may be thought of as an upper bound. Likewise, microcrack twisting along the extension path cannot be captured. Another limitation of the model is the element size required for realistic interface parameters (i.e. $T_{\max}$ and K_{IC}) that plays an important role in selecting the size of the representative volume element. For some cases, this computational cell depends on the conditions of the experiments, periodicity of the microstructures, possible nucleation sites, crack propagation speed, etc. Despite these limitations, the numerical results obtained with this model were not only in good agreement with the experiments, but also were used to explain several microscopic failure mechanisms that have never been quantified before through other mathematical models. 3-D simulations based on the same micromechanical model should basically confirm our mechanistic findings.

Acknowledgements—The authors acknowledge ARO and DoD HPCMP for providing supercomputer time on the 128 processors Origin 2000 at the Naval Research Laboratory — DC (NRL-DC). This research was supported by the National Science Foundation through Career Award Nos. CMS 9523113, CMS-9624364, the Office of Naval Research YIP through Award No. N00014-97-1-0550, the Army Research Office through ARO-MURI Award No. DAAH04-96-1-0331 and the Air Force Office of Scientific Research through Award No. F49620-98-1-0039.

REFERENCES

1. Raiser, G., Clifton, R. J. and Ortiz, M., *Mech. Mater.*, 1990, **10**, 43.
2. Raiser, G., Wise, J. L., Clifton, R. J., Grady, D. E. and Cox, D. E., *J. Appl. Phys.*, 1994, **75**(8), 3862.
3. Raiser, G. F., Dynamic failure resistance of ceramics and glasses. PhD thesis, Brown University, Providence, RI, 1993.
4. Espinosa, H. D., Raiser, G., Clifton, R. J. and Ortiz, M., *J. Hard Mater.*, 1992, **3**, 285.
5. Espinosa, H. D., Micromechanics of the dynamic response of ceramics and ceramic composites. PhD thesis, Brown University, Providence, RI, 1992.
6. Espinosa, H. D. and Nemat-Nasser, S., in *Handbook*, Vol. 8, ed. S. Lampan. ASM, 2000.
7. Simha, C. H. M., Bless, S. J. and Brar, N. S., in *Dynamic Failure of ad99.5 Alumina*. 1995, pp. 195–202.
8. Addessio, F. L. and Johnson, J. N., *Report LA-UR-89-2651*. Los Alamos National Laboratory, Los Alamos, NM, 1999.
9. Curran, D., Seaman, L., Cooper, T. and Shockey, D., *Int. J. Impact Engng.*, 1990, **13**, 53.
10. Rajendran, A. M., *Air Force Report WL-TR-92-4006*. Wright-Patterson Air Force Base, Ohio, 1992.
11. Espinosa, H. D., *Int. J. Solids Struct.*, 1995, **32**, 3105.
12. Johnson, G. R. and Holmquist, T. J., in *Shock-wave and High Strain Rate Phenomena in Materials*, ed. M. A. Meyers, L. E. Murr and K. P. Staudhammer. Marcel Dekker, New York, 1992, p. 1075i.
13. Gailly, B. and Espinosa, H. D., *Int. J. Numer. Meth. Engng.*, 2001, accepted for publication.
14. Camacho, G. T. and Ortiz, M., *Int. J. Solids Struct.*, 1996, **33**, 2899.
15. Ortiz, M. and Pandolfi, A., *Int. J. Numer. Meth. Engng.*, 1999, **44**(9), 1267.
16. Espinosa, H. D., Zavattieri, P. D. and Dwivedi, S., *J. Mech. Phys. Solids*, 1998, **46**(10), 1909.
17. Xu, X. -P. and Needleman, A., *Int. J. Fract.*, 1995, **74**, 253.
18. Miller, O., Freund, L. B. and Needleman, A., *Int. J. Fract.*, 1999, **96**(2), 101.
19. Ghosh, S., Nowak, Z. and Lee, K., *Composite Sci. Technol.*, 1997, **57**, 1187.
20. Ortiz, M. and Suresh, S., *J. Appl. Mech.*, 1993, **60**, 77.
21. Onck, P. and Van der Giessen, E., *Mech. Phys. Solids*, 1999, **47**, 99.
22. Zhai, J. and Zhou, M., *Int. J. Fract.*, 2000, **101**(1-2), 161–180.
23. Helms, K. L. E., Allen, D. H. and Hurtado, L. D., *Int. J. Fract.*, 1999, **95**, 175.
24. Ostoja-Starzewski, M. and Wang, X., *Comput. Methods Appl. Mech. Engng.*, 1999, **168**, 35.
25. Wu, M. and Niu, J., *Mech. Mater.*, 1995, **20**, 9.
26. Kim, B. -N., Wakayama, S. and Kawahara, M., *Int. J. Fract.*, 1996, **75**, 247.
27. Zavattieri, P. D., Rafhuram, P. V. and Espinosa, H. D., *J. Mech. Phys. Solids*, 2001, **49**(1), 27.
28. Zavattieri, P. D., Espinosa, H. D., *Comput. Meth. Appl. Mech. Engng*, 2001, submitted for publication.
29. Tvergaard, V., *Mater. Sci. Engng*, 1990, **A125**, 203.
30. Espinosa, H. D., Zavattieri, P. D. and Emore, G. L., *Mech. Mater. (special issue)*, 1998, **29**, 275.
31. Espinosa, H. D., Dwivedi, S. and Lu, H. -C., *Comput. Meth. Appl. Mech. Engng.*, 2000, **189**, 259.
32. Espinosa, H. D., Raiser, G., Clifton, R. J. and Ortiz, M., *J. Appl. Phys.*, 1992, **72**, 3451.
33. Zavattieri, P. D., Computational modeling for bridging size scales in the failure of solids. PhD thesis, Purdue University, West Lafayette, IN, 2000.
34. Hearmon, R. F. S., *Adv. Phys.*, 1956, **5**, 323.
35. Clifton, R. J. and Sundaram, S., *Mech. Mater.*, 1998, **29**(3-4), 233.
36. Lee, Y. and Prakash, V., *Int. J. Solids Struct.*, 1999, **36**, 3293.
37. Xu, X. -P. and Needleman, A., *J. Mech. Phys. Solids*, 1994, **42**(9), 1397.